Chemical Geology 624 (2023) 121414

Contents lists available at ScienceDirect

Chemical Geology

journal homepage: www.elsevier.com/locate/chemgeo

A common magma source for plutonic and volcanic rocks of The Geysers geothermal field, California: Volume and intrusive history derived from zircon

Carlos A. Angeles-De La Torre[a,*], Axel K. Schmitt[a,b], Oscar M. Lovera[c], Henja Gassert[a], Axel Gerdes[d,e], Janet C. Harvey[a]

[a] Institut für Geowissenschaften, Universität Heidelberg, Germany,
[b] John de Laeter Centre, Curtin University, Australia
[c] Department of Earth, Planetary, and Space Sciences, University of California, United States,
[d] Institut für Geowissenschaften, Goethe Universität Frankfurt am Main, Germany
[e] Frankfurt Isotope and Element Research Center (FIERCE), Goethe University, Frankfurt, Germany

ARTICLE INFO

Keywords:
Quaternary
Magmatism
Geothermal energy
Trace elements
Oxygen isotopes
Hafnium isotopes
Zircon

ABSTRACT

The Geysers Plutonic Complex (GPC) in the California Coast Ranges underlies one of the world's premier geothermal resources. The GPC consists of three major intrusive phases, orthopyroxene-biotite microgranite porphyry, orthopyroxene-biotite granite, and hornblende-biotite-orthopyroxene granodiorite (in sequence of emplacement). These are nearly coeval and compositionally equivalent to lavas of the overlying Cobb Mountain Volcanic Center which includes (from older to younger) rhyolite of Alder Creek, dacite of Cobb Mountain, and dacite of Cobb Valley. Zircon from GPC plutonic and associated volcanic rocks were analyzed at high spatial resolution for their trace element abundances along with oxygen and hafnium isotopic compositions. Pronounced negative Eu anomalies and high incompatible trace element (e.g., Y, Hf, and U) abundances in zircon along with low Ti-in-zircon temperatures reveal that the GPC microgranite porphyry magma was more evolved than GPC granite and granodiorite. Isotopically, GPC microgranite porphyry, granite, and granodiorite zircon crystals closely overlap ($\delta^{18}O = +4.76$ to $+9.18$; $\varepsilon Hf = +1.4$ to $+10.7$), but a subpopulation with elevated $\delta^{18}O$ (~ 8.05) and lower εHf (~ 4.4) is only present in GPC granite and granodiorite. Zircon from coeval volcanic units share this dichotomy, with a dominant population at ($\delta^{18}O = +4.92$ to $+9.38$; $\varepsilon Hf = +3.4$ to $+11.3$) and a generally minor population with elevated $\delta^{18}O$ and low εHf, which is particularly prominent in dacite of Cobb Valley. Anticorrelated $\delta^{18}O$ and εHf values indicate progressive assimilation of Franciscan Complex basement rocks, but fractional crystallization was decoupled from crustal assimilation. Together with published U-Th-Pb geochronology, these data reveal distinct degrees of crust-mantle interaction and constrain the thermochemical conditions during different stages in the evolution of a composite intrusive body that fed the GPC and contemporaneous volcanoes. A thermal model for such a body emplaced at ~7 km depth quantitatively matches the GPC zircon age distribution when magma accumulation started at low recharge rates (0.1 km^3/ka), intermittently peaked during a brief flare-up (4 km^3/ka for 50 ka), and then returned to a low recharge flux (0.1 km^3/ka). This model also qualitatively explains the initial presence of small-volume, highly evolved melts forming the microgranite porphyry, followed by massive emplacement of less evolved magmas forming the GPC granite-granodiorite complex. During this second stage, crustal assimilation locally intensified due to prior thermal priming of the country rock. The total injected magma volume into the upper-crustal reservoir between c. 2.1 and 1.1 Ma amounts to ~300 km^3, which is about three to four times the known volume from geothermal well penetration into the GPC. The accumulation of large volumes of silicic magma along the western North American continental margin in the wake of the northward migrating Gorda slab edge thus appears limited to a brief (c. 50 ka) pulse of high magma influx from the mantle that was pre- and post-dated by protracted low-flux magmatism.

* Corresponding author.
E-mail address: Carlos.Angeles@geow.uni-heidelberg.de (C.A. Angeles-De La Torre).

https://doi.org/10.1016/j.chemgeo.2023.121414
Received 15 December 2022; Received in revised form 3 March 2023; Accepted 5 March 2023
Available online 13 March 2023
0009-2541/

1. Introduction

1.1. Crystals and the volcanic-plutonic connection

Complex crystal origins are increasingly recognized for magmatic rocks, and therefore polygenetic crystal populations can track the thermal and chemical evolution of magmas over a significant part of their lifetime, in some cases from magmatic sources to emplacement at the surface (e.g., Barth and Wooden, 2010). Accessory mineral geochronology is particularly important to identify crystals that can be unequivocally linked to processes such as magma emplacement, cooling, and differentiation (e.g., Chelle-Michou et al., 2014). U-Th-Pb zircon ages in intermediate to evolved subalkaline volcanic rocks nearly universally reveal protracted crystallization prior to eruption (e.g., Simon et al., 2005), but surprisingly, truly xenocrystic zircon is often scarce (e.g., Kern et al., 2016). This suggests that evolved melts had precursors that were originally zircon undersaturated, a condition which facilitates resorption of xenocrystic zircon during the early stages of magmatic differentiation. Crystal recycling from different parts of an evolving plutonic complex has been recognized in volcanic zircon crystals based on a comparison with cogenetic plutonic enclaves in pyroclastic deposits (Schmitt et al., 2010; Barboni et al., 2016). Although plausible, it is difficult to demonstrate a correlation between volcanic and plutonic crystals in general, because either the subvolcanic plutons are concealed, or the volcanic counterparts have been eroded. Moreover, cogenetic plutonic enclaves in volcanic rocks remain ambiguous as a probe into the underlying intrusive complex because these are dislodged from their original location, and their exact provenance is thus uncertain.

The Geysers-Cobb Mountain system in the California Coast Ranges is a rare example of cogenetic volcanic and plutonic rocks that are accessible for direct comparison due to shallow emplacement of a pluton underneath a volcanic field, with the entirely subsurface pluton being drilled by numerous geothermal wells (Fig. 1). Wells up to nearly 4 km deep have penetrated a shallow composite pluton termed the Geysers Plutonic Complex (GPC), informally known as the "felsite", which encompasses subintrusions of orthopyroxene-biotite microgranite porphyry, orthopyroxene-biotite granite, and hornblende-biotite-orthopyroxene granodiorite. The geothermal reservoir ("The Geysers") hosted by the GPC and its caprock is one of the world's most productive, with an installed capacity of ~1.5 GW (Bertani, 2012). Its heat source has been attributed to unidentified intrusions within or below the known GPC (Dalrymple et al., 1999; Donnelly et al., 1981; Hulen et al., 1997; Kennedy and Truesdell, 1996; Peacock et al., 2020; Schmitt et al., 2003a; Schriener Jr and Suemnicht, 1980; Stimac et al., 2001). Volcanic rocks exposed nearby in the Cobb Mountain Volcanic Center (CMVC)

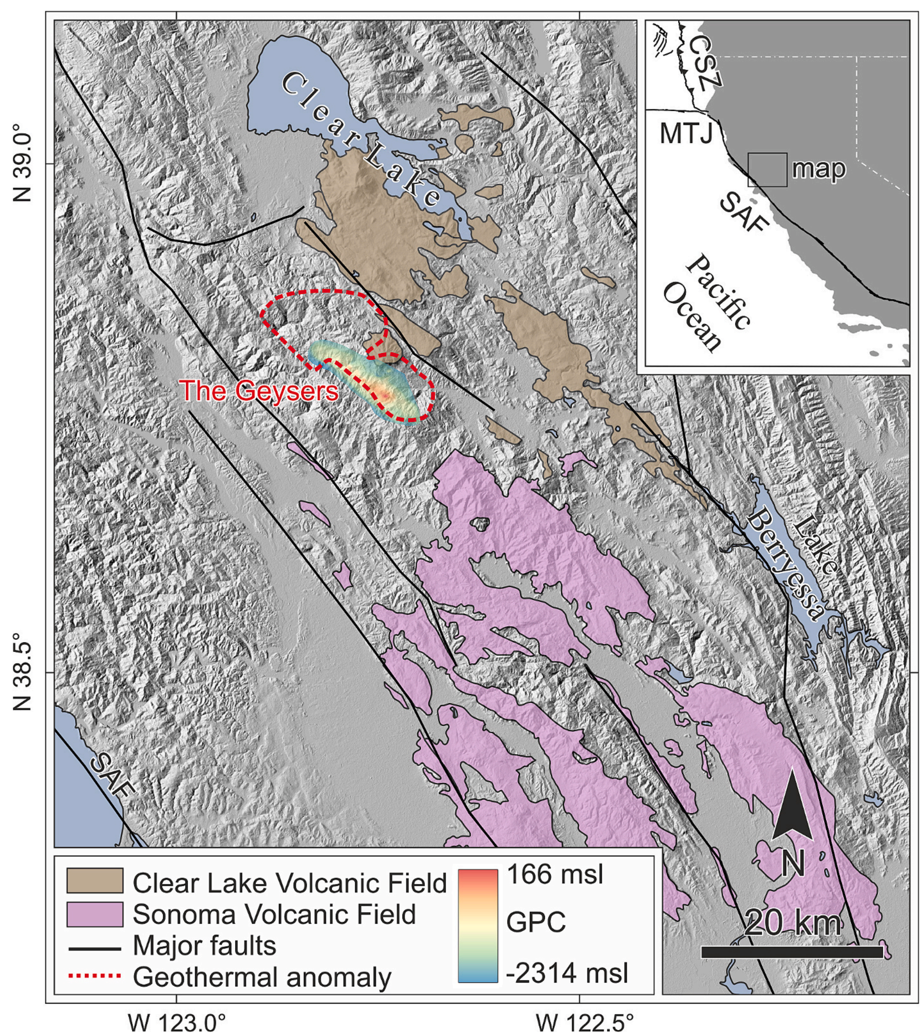

Fig. 1. Simplified geologic map showing extent of the Clear Lake volcanic field, the Sonoma volcanic field, and the outline of "The Geysers" geothermal anomaly with the subsurface Geysers Plutonic Complex (GPC). Surface of the GPC is stated in meters relative to sea level (msl). Abbreviations: MTJ = Mendocino Triple Junction; CSZ = Cascadia Subduction Zone; SAF = San Andreas Fault. Hillshade derived from SRTM 3 arcsecond DEM. (NASA JPL, 2018); geology after Jennings et al. (2010).

comprise rhyolite of Alder Creek (ACR), rhyodacite of Cobb Mountain (CMD), and dacite of Cobb Valley (CVD). ACR yielded a widely used Quaternary reference sanidine for $^{40}Ar/^{39}Ar$ geochronology, where the dominant population of single-crystal sanidine ages defines an eruption age of 1.1864 Ma (Jicha et al., 2016; Rivera et al., 2013). However, a tail of older sanidine crystals was detected in several studies and interpreted as recycling from plutonic rocks (Rivera et al., 2013). Zircon defines an even wider-ranging spectrum of ages, with the youngest U-Th-Pb zircon ages overlapping with the $^{40}Ar/^{39}Ar$ sanidine eruption age, but many zircon crystals are also significantly older, and these have also been interpreted as inherited from older intrusions in the magma source region (Rivera et al., 2013; Schmitt et al., 2003a, 2003b).

While earlier studies emphasized a strong link between GPC rocks and the CMVC, they did not resolve (1) whether zircon ages and compositional trends correspond between volcanic and plutonic rocks, or if they evolved distinctly, (2) how fractional crystallization and assimilation progressed in different parts of a potentially common magma source, and (3) how the reservoir from which GPC and CMVC magmas were extracted waxed and waned in time and space. Zircon is particularly useful to provide new perspectives for answering these questions because it is chemically and physical resilient with negligible diffusion of most components even at magmatic temperatures (Cherniak and Watson, 2003; Page et al., 2007; Peck et al., 2003) or in agressive hydrothermal environments (e.g., Wilson et al., 2008; Milicich et al., 2013). Hence, it records the thermal and chemical evolution of magma with absolute time information, and it contains abundant O and Hf where isotopic compositions are clear indicators for different mantle vs. crustal contributions (e.g., Kemp et al., 2007; Payne et al., 2016; Scherer et al., 2007, and references therein). Furthermore, recent studies have laid out the potential of zircon thermal models to quantify extensive parameters such as rates and durations of magma inputs by matching observed age distributions and temperatures of zircon from volcanic or plutonic rocks with the cooling timescales predicted for magma reservoirs undergoing episodic recharge (Caricchi et al., 2014; Friedrichs et al., 2021; Lukács et al., 2021; Tierney et al., 2016; Weber et al., 2020).

This study compares trace element, $\delta^{18}O$, and εHf data for zircon from volcanic and plutonic samples of the GPC-CMVC complex using crystals previously dated in Schmitt et al. (2003a, 2003b). We confirm that volcanic and plutonic zircon formed under similar conditions in a common source magma. This magma evolved via crustal assimilation and fractional crystallization, which however, were largely decoupled, and only crystals from the younger and more voluminous GPC granite-granodiorite stage became subsequently recycled during volcanic eruptions. Modelling of magma fluxes into the source system over the duration recorded by zircon between c. 2.1 and 1.1 Ma reveals a progression from slow-paced and gradual magma build up to a brief interval of peak accumulation, and subsequent return to incremental addition at low recharge rate.

1.2. Geological setting and previous geochronology

Covering an area of ~400 km^2, the Clear Lake volcanic field is considered the youngest and northernmost of a series of volcanic centers in the eastern Coast Ranges of California (Fig. 1; Donnelly et al., 1981; Fox et al., 1985). The Coast Ranges crust mainly consists of a heterogeneous assemblage of the Franciscan Complex comprising igneous rocks, metamorphosed graywacke, serpentinite, as well as sedimentary rocks, mostly turbiditic metasandstone and argillite (Aalto, 2014; Ernst, 2015; McLaughlin, 1981; Wakabayashi, 2015). Seismic studies indicate crustal thicknesses of 24–30 km for the immediate Clear Lake area of which 12–18 km belong to the Franciscan Complex overlying gabbroic rocks (Castillo and Ellsworth, 1993; Mooney and Weaver, 1989). Magmatism in the Clear Lake area began at about 2.1 Ma and progressively became younger to the north as consequence of the northward migration of the Mendocino triple junction (Dickinson and Snyder, 1979; Donnelly et al., 1981; Hearn Jr et al., 1981; Johnson and O'Neil, 1984). A transcrustal complex of magma bodies was emplaced underneath the entire Clear Lake volcanic field based on thermobarometry from metamorphic xenoliths indicating magma ponding at 780–900 °C and 400–600 MPa (12–18 km depth; Stimac et al., 2001). The deeper parts of these magma systems were dominated by mafic intrusions where crustal contamination occurred, and from which hybridized, silicic magma subsequently migrated to shallower levels (Hammersley and DePaolo, 2006; Stimac and Pearce, 1992). Intermediate to evolved magmas originated from hybridized mantle-crustal rocks based on their mixed stable ($^{18}O/^{16}O$) and radiogenic ($^{87}Sr/^{86}Sr$, $^{143}Nd/^{144}Nd$, $^{206}Pb/^{204}Pb$) isotopic inventory. Magma hybridization and subsequent melt evolution occurred in multiple stages involving early assimilation and fractional crystallization (AFC) at depth, followed by shallow fractional crystallization (Hammersley and DePaolo, 2006; Johnson and O'Neil, 1984; Schmitt et al., 2006).

The southwestern zone of the Clear Lake volcanic field includes "The Geysers", one of the most productive geothermal fields worldwide. It is underlain by the GPC (Fig. 2) which, based on geothermal drill well penetration, mainly consists of three petrologically distinct units that also differ in age (from old to young; Fig. 3): a shallow (~0.2–1.2 km depth below the surface) orthopyroxene-biotite microgranite porphyry with an U-Th-Pb zircon average age of 1.75 ± 0.01 Ma, and a deeper (~1.1–2.8 km) complex of orthopyroxene-biotite granite (1.27 ± 0.01 Ma), and hornblende-biotite-orthopyroxene granodiorite (1.24 ± 0.01 Ma; Hulen and Nielson, 1993; Norton and Hulen, 2001; Schmitt et al., 2003b). Assuming that the complex extends to a depth of −3000 m relative to sea level (msl) yields a conservative volume estimate of ~75 km^3 for the GPC (this study, based on interpolation of depth to the GPC provided by CALPINE, pers. comm.). Closely associated with the GPC are Quaternary volcanic rocks that cover the full compositional range from basalt to rhyolite. The oldest units within the area of the steam field comprise andesite of Ford Flat and basalt of Caldwell Pines with reported whole-rock K-Ar ages of 1.71 ± 0.21 and 1.66 ± 0.12 Ma, respectively (Donnelly et al., 1981). Lavas and minor pyroclastic deposits of intermediate–rhyolitic composition of the CMVC totaling ~5 km^3 are exposed above the eastern margin of the steam field (Fig. 2). The CMVC was active at 1.1850 ± 0.0016 Ma (ACR; Rivera et al., 2013), 1.10 ± 0.02 Ma (CMD), and 1.00 ± 0.05 Ma (CVD; Schmitt et al., 2003a), with zircon crystallization ages generally predating the respective eruption ages by up to several hundreds of ka (Fig. 3; Rivera et al., 2013). Older and younger volcanic rocks are mapped as rhyolite of Pine Mountain ($^{40}Ar/^{39}Ar$ sanidine age = 2.17 ± 0.02 Ma) and dacite of Tyler Valley ($^{40}Ar/^{39}Ar$ sanidine age = 0.67 ± 0.01 Ma) towards the southeast and northwest of the GPC, respectively (Schmitt et al., 2003a). Only the Hachimantai geothermal area, Japan, with the subsurface Kakkonda pluton, is comparable to the GPC-CMVC in providing access to a Quaternary pluton with cogenetic volcanic rocks preserved at the surface (e.g., Ito et al., 2013).

The recent Geysers steam field is a vapor-dominated hydrothermal system with temperatures varying from ~240 °C in the southeast and increasing with depth up to ~340 °C towards the northwest. Heat flow in the steam field peaks at values of up to 500 mW/m^2 which even exceeds the already elevated heat flow of the Clear Lake volcanic field by a factor of three (Walters and Combs, 1992). Based on K-feldspar $^{40}Ar/^{39}Ar$ incremental-heating ages, the GPC had cooled to <350 °C by c. 0.9 Ma (Dalrymple et al., 1999) when a fluid-dominated hydrothermal system became established (Hulen et al., 1997; Hulen and Nielson, 1995; Moore et al., 2000; Moore and Gunderson, 1995). As indicated by vein adularia $^{40}Ar/^{39}Ar$ ages combined with fluid inclusion data, temperatures cooled down to <300 °C at c. 0.26 Ma, when the shallow hydrothermal system became vapor-dominated (Hulen et al., 1997). Elevated $^{3}He/^{4}He$ (6.8–8.3 times relative to atmosphere) and Cl abundances in modern geothermal fluids indicate a young magmatic intrusion that provides the heat for the current steam field (Beall and Wright, 2010; Donnelly et al., 1981; Kennedy and Truesdell, 1996; Stimac et al., 2001). Because the highest temperatures in the modern geothermal system are

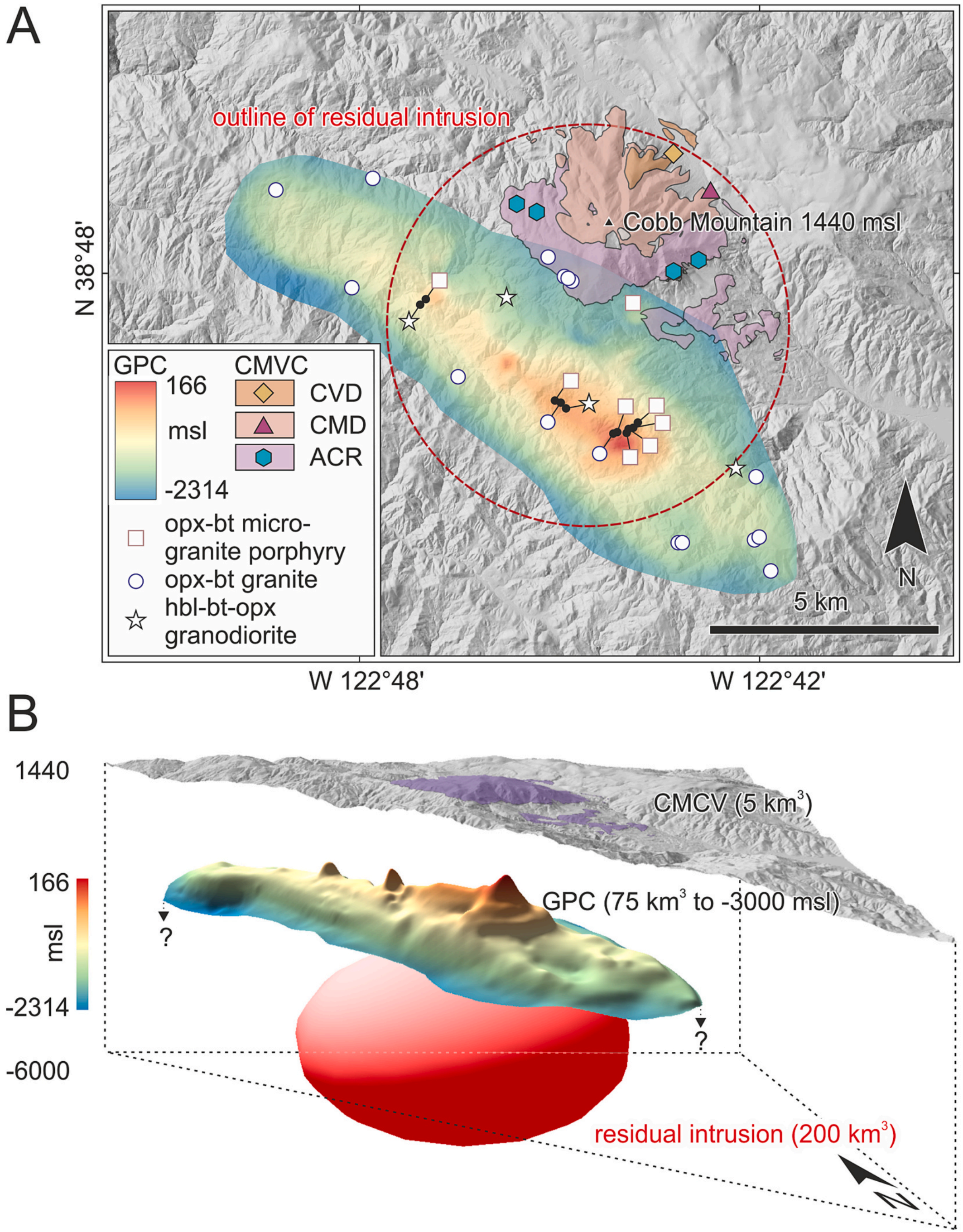

Fig. 2. A) Overview map of the Cobb Mountain Volcanic Complex and the underlying Geysers Plutonic Complex. Sample locations (surface for the CMVC and geothermal wells for GPC; Schmitt et al., 2003a, 2003b) are indicated. Outline of the modelled residual intrusive system representing the common magma source after extraction of the GPC and volcanic units based on zircon age modelling is plotted for comparison (see text). B) Surface topography, top of the GPC and the underlying modelled intrusive ellipsoid in a 3D perspective view. Illumination from the NW. Hillshade derived from U.S. Geological survey 1/3 arc sec DEM (U.S. Geological Survey, 2017). Depth to top of GPC interpolated from points provided by CALPINE (pers. comm.).

encountered in the NW Geysers area, a recent intrusion along with a putative partial melt zone at >7 km extending in a NE direction towards the Clear Lake volcanic field has been proposed (Peacock et al., 2020), although plutonic rocks of such young age have yet to be drilled.

2. Material and methods

2.1. Sample origins and processing

All zircon crystals were previously dated using U-Th-Pb geochronology (Schmitt et al., 2003a, 2003b). New U-Th-Pb zircon ages for a thin pyroclastic deposit on the SE flank of Cobb Mountain (sample CM-04-01 from the Anderson Flat area) that underlies ACR lava and was mapped as unit "rap" in Hearn et al. (1995) are included in Fig. 3 and the supplementary data (Table S1). Lava was collected as kg-sized specimens at surface outcrops, crushed, and sieved. For the pyroclastic sample CM-04-01, a composite sample of several cm-sized lapilli was processed similar to the lava samples. Most plutonic samples originated as ~10–100 g of mm-sized air drill cuttings which were gently crushed on a steel plate (Schmitt et al., 2003a, 2003b). Zircon crystals were

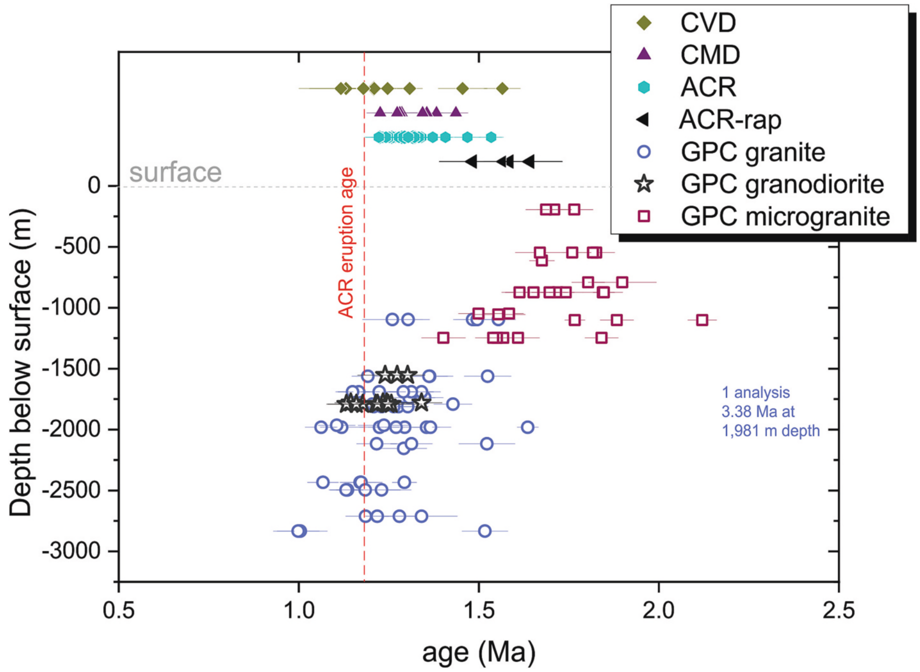

Fig. 3. SIMS U-Th-Pb zircon ages (from Schmitt et al., 2003a, 2003b) for the GPC against depth below surface (open symbols), and for the CMVC (filled symbols) in chronostratigraphic order. Data were screened for >85% radiogenic ^{206}Pb.

separated from sieved material <250 μm using conventional density and magnetic enrichment, followed by hand-picking and mounting for optical and cathodoluminescence imaging and high spatial resolution (secondary ionization mass spectrometry, SIMS, and laser ablation inductively coupled plasma mass spectrometry, LA-ICP-MS) analysis. Surfaces were gently reground and polished between analyses.

2.2. SIMS and LA-ICP-MS analysis of zircon

Zircon U-Th-Pb analyses were carried out at University of California Los Angeles on a CAMECA ims1270 as outlined in Schmitt et al. (2003a). Trace element and oxygen isotope analysis of zircon was performed using the CAMECA ims 1280-HR at the Heidelberg Ion Probe (HIP) laboratory following methods described in Schmitt et al. (2017) with cathodoluminescence (CL) imaging carried out using a Gatan MiniCL on a Leo 440 scanning electron microscope. For trace element analysis, a ~ 15 nA $^{16}O^-$ primary beam was focused into a ~ 20 μm Köhler-illuminated spot on the re-polished zircon surface, targeting the same domains previously analyzed for U-Th-Pb (often CL-dark interiors in the interiors). Using energy filtering (−100 eV), secondary ions were detected at low (m/Δm = 2000) mass resolution. Molecular interferences of light rare earth element (LREE) oxides on atomic ion species of the middle and heavy rare earth elements (MREE, HREE) were subtracted for $^{156}Gd^+$ ($^{140}CeO^+$), $^{158}Gd^+$ ($^{142}CeO^+$, $^{142}NdO^+$), $^{159}Tb^+$ ($^{143}NdO^+$), $^{165}Ho^+$ ($^{149}SmO^+$), ^{169}Tm + ($^{153}EuO^+$), $^{172}Yb^+$ ($^{156}GdO^+$), and $^{175}Lu^+$ ($^{159}TbO^+$) using correction factors for oxide and hydride species determined on doped glasses. Relative sensitivity factors were calibrated on NIST SRM 610 (Pearce et al., 1997), and accuracy was monitored by analyzing 91500 reference zircon (Wiedenbeck et al., 2004). All data on unknowns were screened for anomalies in the light rare earth element index (LREE-I = Dy/Nd + Dy/Sm) and La abundances, discarding all values >30 and > 0.1, respectively (Bell et al., 2019), which are interpreted as indicating overlap onto non-zircon phases (e.g., apatite, glass, or oxide inclusions); the full data set, including values for the secondary zircon reference, is presented in the supplement (Fig. S1, Table S2). Temperatures for zircon crystallization based on Ti abundances in zircon (TiZr) were obtained following the equation in Ferry and Watson (2007) for quartz-saturated, but rutile-absent melt using activities of $\alpha_{SiO2} = 1$ and $\alpha_{TiO2} = 0.55$, consistent with Rivera et al. (2013) in their trace element study of ACR zircon. Analytical uncertainties translate into temperature uncertainties of <10 °C based on the external reproducibility of Ti analysis of 91500 zircon reference (4.7 ± 0.3 ppm; 1 SD; n = 9). For oxygen isotope (^{16}O and ^{18}O) analysis, a ~ 2 nA Cs^+ beam in critical illumination was rastered over a 10 × 10 μm^2 area on zircon. Intensities of $^{16}O^-$, $^{16}OH^-$, and $^{18}O^-$ were simultaneously monitored in three Faraday detectors and corrected for detector yield and average backgrounds recorded prior to each analysis. Reference zircon AS3 ($\delta^{18}O$ = +5.34 ‰; Trail et al., 2007; all values reported on the VSMOW scale) was intermittently analyzed to determine instrumental mass fractionation factors that were applied to unknowns. Reproducibility of the sliding average of multiple AS3 analyses per analysis day was between 0.14 and 0.22 ‰ (1SD). Because targeted zircon domains are typically much larger than the ~5 μm thick surface layer lost due to resurfacing after SIMS analysis, age, trace element, and oxygen isotope results can be reliably correlated.

For Hf isotope measurements, a ThermoScientific NEPTUNE Plus multicollector (MC)-ICP-MS system at FIERCE, Goethe University Frankfurt coupled to a RESOlution S155 193 nm ArF Excimer (Resonetics) laser system was used as described in Gerdes and Zeh (2006, 2009). Laser spots with lateral dimension of ~35 μm in diameter were set on top of SIMS analysis pits. Each grain was ablated for 38 s using a fluence of 4 J cm^{-2} and a frequency of 8 Hz, which resulted in an ablation rate of 0.65 μm s^{-1}, or ~ 25 μm total depth. An exponential law with ^{179}Hf/^{177}Hf value of 0.7325 was used for instrumental mass bias corrections. For Yb isotopes, instrumental mass bias was corrected using the Hf mass bias of the individual integration step multiplied by a daily βHf/βYb offset factor (Gerdes and Zeh, 2009). All data were adjusted relative to the JMC475 ^{176}Hf/^{177}Hf ratio = 0.282160 and quoted uncertainties are quadratic additions of the within-run precision of each analysis and the reproducibility of JMC475 (2SD = 0.0028%, n = 8). Secondary zircon references Temora and GJ-1 analyzed in the same analytical session agree with published values (see full data in supplement).

2.3. Numerical modelling

Zircon crystallization in a magmatic reservoir open for recharge was modelled modifying the approach of Tierney et al. (2016) to accommodate multiple magma extraction events. This model is based on the equations for recharge-assimilation-fractional crystallization (Spera and Bohrson, 2001) and has a grid resolution of 0.1 × 0.1 km over a 20 × 60 km (width × depth) rectangle representing a block of upper–middle crust. Constant heat flow through the base and surface is maintained during the model run. Magma recharge occurs every 5000 years into the center of an ellipsoidal magma chamber, which retains its originally defined aspect ratio (here: height to width ratio = 0.6). The temperature of the cells as they are displaced outward from the center of the intrusion is monitored continuously with each recharge step, along with zircon production in cells that are in a temperature range where zircon saturation is reasonably expected for subalkaline melt compositions and where the magma is above the solidus (i.e. 800–700 °C; Tierney et al., 2016). The relative amounts of zircon crystallized in these cells are integrated for the time of magma extraction. Intrusion depths and temperatures of the recharge magma and the country rock are prescribed, along with a small, generally insignificant initial intrusion volume (5 km^3). Magma input rates and timing are then varied to compute a zircon age distribution that is to be matched to that detected in volcanic or plutonic samples. Model results are evaluated against observations using cumulative probability density functions and the age difference (Δt) between the 16–84% percentiles of the model and data distributions.

As the depth of intrusion, we adopted 7 km in all models as this is intermediate between the lower limit of the known GPC depth (~3 km) and the top of the inferred mid-lower crustal mafic magma storage zone (~12 km; Stimac and Pearce, 1992). A similar depth was previously

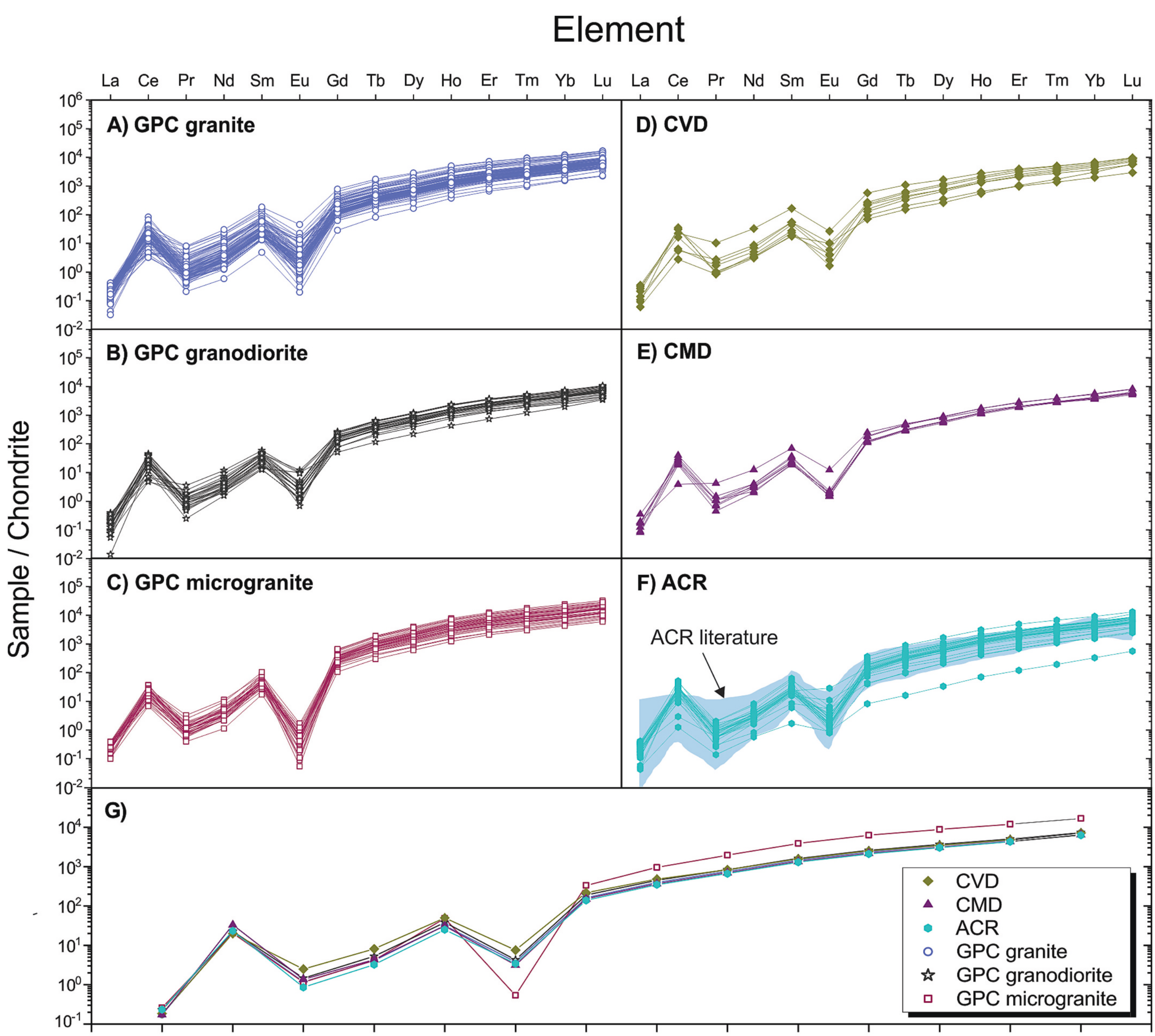

Fig. 4. Chondrite normalized REE abundances in zircon for the GPC (A to C), CMVC (D to F) and average compositions (G) determined by SIMS. LA-ICP-MS data for ACR (blue field) from Rivera et al. (2013) are shown for comparison. All data on unknowns with the exception of the literature field were screened for contamination by non-zircon phases using the LREE-I and La filters (see text). (For interpretation of the references to colour in this figure legend, the reader is referred to the web version of this article.)

proposed for the magma reservoir of nearby Mt. Hannah volcano (Isherwood, 1981; McLaughlin, 1981), and corresponds to the low-resistivity domain detected underneath the Northwest Geysers steam field and adjacent parts of the Clear Lake volcanic field (Peacock et al., 2020). Recharge temperatures of 1000, 1100, and 1200 °C were explored. The lower bound represents the maximum temperature for silicic magmas in the Coast Ranges, whereas a maximum corresponds to regional mafic magmas typically estimated at 1150–1170 °C (Stimac et al., 2001). Geothermal gradients for the pre-intrusion crust are between 30 and 40 °C/km, similar to those previously used in thermal models for the region (Norton and Hulen, 2001; Schmitt et al., 2006). Modelled zircon age distributions were then compared to average zircon ages previously determined in Schmitt et al. (2003b).

3. Results

3.1. Trace elements

All zircon crystals from the GPC and related volcanic units exhibit pronounced negative Eu and positive Ce anomalies. Overall higher HREE abundances and lower Eu/Eu* set apart the microgranite porphyry from the other plutonic and volcanic units (Fig. 4). Microgranite porphyry zircon on average displays very low Eu/Eu* = 0.0045, whereas zircon from the GPC granite and granodiorite as well as those from the volcanic units have Eu/Eu* mostly between 0.01 and 0.1 (Fig. 5 A). Moreover, Eu/Eu* negatively correlates with Hf and positively with

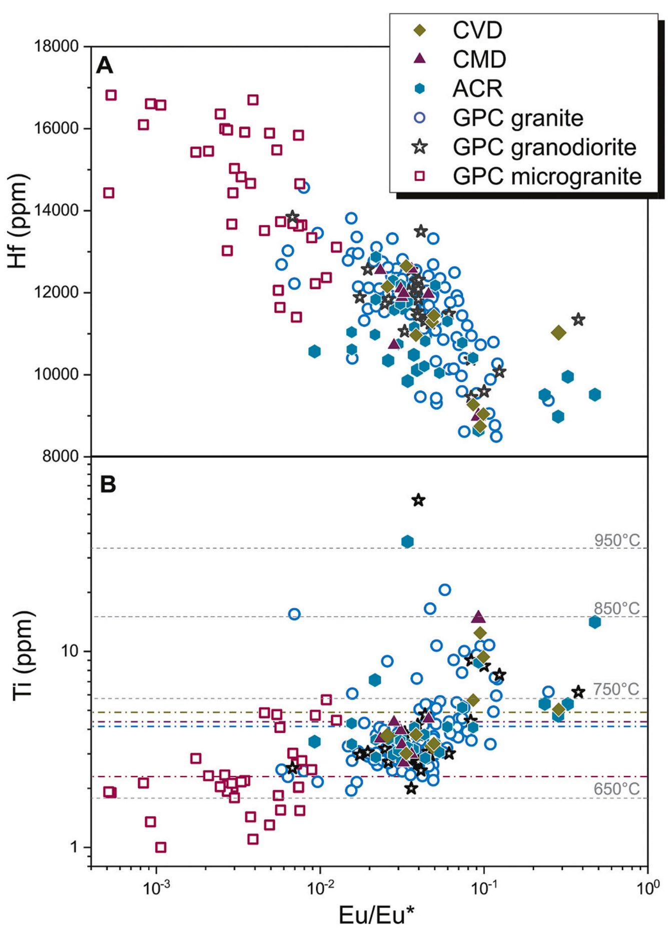

Fig. 5. Trace element Hf abundances against Eu/Eu* (A) and Ti abundances against Eu/Eu* (B) for GPC and CMVC zircon determined by SIMS. Right axis in (B) indicates Ti-in-zircon temperatures calculated for a(SiO_2) = 1 and a(TiO_2) = 0.55 (see text), average temperatures of individual units are shown by dashed-dot lines.

Ti abundances in zircon (Fig. 5 A, B). This relation holds for the overall zircon population, in which the micrograníte stands out as having the highest Hf and lowest Ti abundances, but also for individual subgroups (e.g., GPC granite), indicating a fractional crystallization trend involving feldspar prior to and during zircon crystallization (e.g., Claiborne et al., 2010). The plot of U against Yb abundances discriminates among different petrogenetic origins of zircon (Grimes et al., 2007), with all zircon from the GPC and CMVC lavas having U/Yb >0.1 indicative of continental crustal sources (Fig. S2). Zircon crystals from the microgranite porphyry display the highest abundances in U (up to 17,400 ppm), whereas zircon from all other units contains U at <7000 ppm (Fig. S3). The exceptions are zircon crystals from the pre-ACR pyroclastic deposit that feature high U abundances similar to GPC microgranite porphyry zircons. On average, TiZr thermometry ranges between ~670 °C for the microgranite porphyry and ~ 720 °C for the GPC granite and granodiorite. Calculated temperatures for CMVC zircon are generally >680 °C; ACR and CMD yielded indistinguishable TiZr averages of ~725 °C, whereas CVD displays the highest average of ~735 °C (Fig. 5 B).

When plotting zircon differentiation indices (e.g., U, Th, Hf abundances or Eu/Eu*) against the age of zircon (Fig. S3), a trend is recognized from the older (c. 1.5–2.1 Ma), shallower, and significantly more evolved microgranite porphyry to the younger, deeper, and less evolved GPC granite-granodiorite as well as the overlying CMVC (c. 1.1–1.5 Ma). Zircon data from ACR reported by Rivera et al. (2013) mimic a similar trend, however, over a briefer timescale between c. 1.15 and 1.33 Ma. GPC granite zircon analyses only rarely overlap in age and composition with those of the shallower micrograníte zircon, suggesting very limited zircon carry over from older to younger parts of the intrusion. Even for the few crystals in the GPC granite for which a micrograníte origin can be inferred, we caution that this could be due to contamination of the drill cuttings from the deeper GPC rocks by the overlying micrograníte porphyry.

3.2. O- and Hf-isotopes

Zircon $\delta^{18}O$ values of all samples vary between +4.8 and + 9.4, with most data above values for zircon crystallized in purely mantle-derived melts (~ + 5.3; Valley et al., 1998). When accounting for $^{18}O/^{16}O$ fractionation between melt and zircon by adding ~1 ‰ to the zircon values (Trail et al., 2009), this range largely overlaps with inferred magma compositions for volcanic rocks from the California Coast Ranges ($\delta^{18}O$ = +8.4 to +10.5 for dacites-rhyolites from Clear Lake) that have been interpreted to be strongly affected by crustal anatexis and assimilation by mantle-derived mafic melts where regional country rock compositions of the Franciscan Complex have $\delta^{18}O$ values of +10 to +16 (Johnson and O'Neil, 1984; Lambert and Epstein, 1992). Essentially the full range in $\delta^{18}O$ is covered by zircon from the GPC granite which displays a bimodal distribution with peaks at +6.4 and + 8.6, whereas GPC micrograníte zircon $\delta^{18}O$ is unimodal, and has a narrower range between +5.5 and + 7.6 (Fig. 6). Volcanic units ACR and CMD mostly overlap with the lower $\delta^{18}O$ cluster in the GPC granite that also encompasses the data for the GPC micrograníte and granodiorite, whereas CVD zircons with one exception match the higher $\delta^{18}O$ cluster (Fig. 6). Overall, the $\delta^{18}O$ and εHf compositions negatively correlate, with again two clusters most prominently displayed in the GPC granite population (peak values at +3.5 and + 7.5 and an overall range from +1.4 to +10.7), and a distribution of the other units that corresponds to that displayed by the $\delta^{18}O$ data (Fig. 6). Although published data for εHf from potential mantle and crustal end-members in the California Coast Ranges are lacking, the negative correlation displayed by zircon in $\delta^{18}O$ and εHf is consistent with mixing or AFC trends frequently observed in continental magmatic settings (e.g., Kemp et al., 2007). For illustration, εHf was calculated from published εNd data and plotted against $\delta^{18}O$ for mixing and AFC between basaltic and crustal end-members (Fig. 6). While such a model can explain the isotopic composition of the source

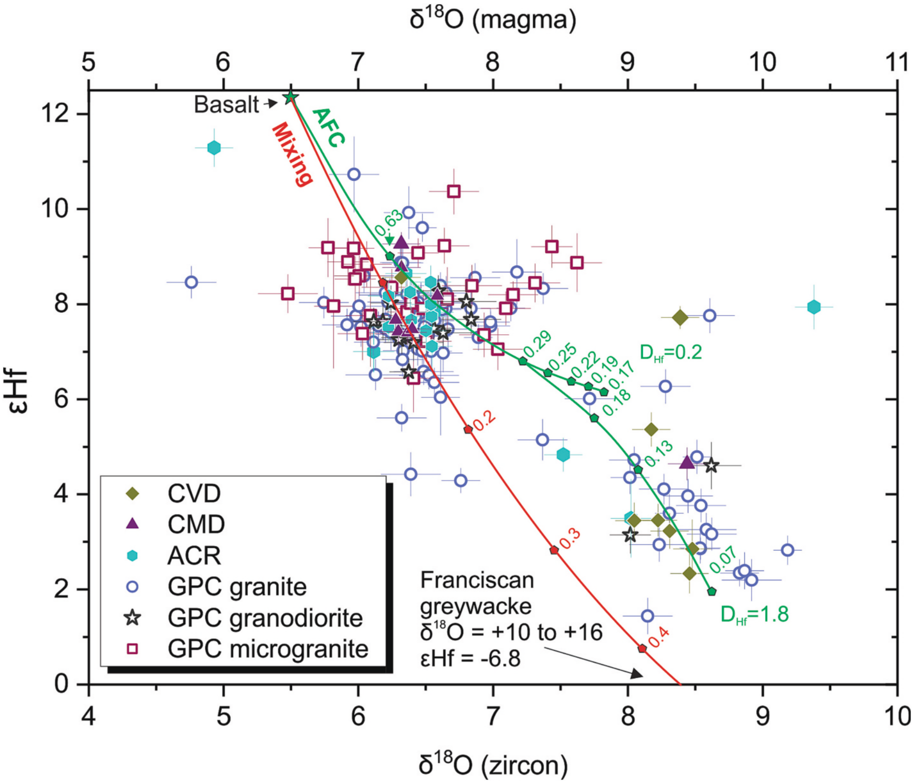

Fig. 6. Covariation diagram of Hf isotopes vs. O isotopes of GPC and CMVC zircon. Lower axis is for zircon values, and upper axis is for magma values based on whole rock data; axes are shifted to accommodate a − 1 ‰ fractionation between zircon and melt (Trail et al., 2009). Curves illustrate mixing and AFC trends between potential mantle (basalt of Caldwell Pines) and crustal (Franciscan Complex graywacke) end-members with numbers indicating fraction of crustal contaminant (mixing) and fraction of melt remaining (AFC). End-member compositions from Johnson and O'Neil (1984) and Schmitt et al. (2006), with εNd values recalculated as εHf according to the global arrays in Chauvel et al. (2008) for the basaltic end-member and Vervoort et al. (2011) for metasediments. Abundances of Hf (estimated from whole rock Zr data assuming chondritic Zr/Hf), and r value (ratio of assimilation to fractionation = 0.2) were adapted from Schmitt et al. (2006). Incompatible behavior of Hf was assumed for fractional crystallization prior to zircon saturation (bulk mineral-melt partitioning coefficient D_{Hf} = 0.2), which corresponds to the initial mafic-intermediate melt evolution, and D_{Hf} = 1.8 after onset of zircon saturation in evolved melts. Bulk D_{Hf} values were adapted from Kemp et al. (2007) for either a zircon-free mineral assemblage, or zircon being present at 0.05%, acknowledging that a constant amount of zircon and the resulting D_{Hf} value are simplifying assumptions as both are expected to vary during magma evolution.

magmas that produced the majority of the GPC and CMVC zircons, a simple single-stage AFC model (where Hf is incompatible with a bulk partition coefficient D_{Hf} = 0.2) would miss the more crustally contaminated zircon population. This suggests that melt evolution occurred in multiple stages, with Hf becoming compatible in evolved melts upon zircon saturation (second-stage AFC curve with a bulk partition coefficient D_{Hf} = 1.8; Fig. 6).

For δ^{18}O vs. Eu/Eu*, two clusters in δ^{18}O are evident, but even the zircon crystals from the microgranite porphyry with the lowest Eu/Eu* display inconspicuously low δ^{18}O (Fig. 7A). In the εHf vs. Hf abundance plot for zircon, the data are broadly correlated, which is, however, opposite to the expected AFC trend where Hf in zircon would increase with increasing fractionation, and εHf would decrease with increasing crustal contamination (Fig. 7A). Hence, isotopic composition and trace element indices for magma differentiation (Eu/Eu*, Hf abundance in zircon) lack the systematic co-variation that is characteristic for AFC (Fig. 7A, B), similar to findings for the bulk composition of evolved rocks in the Clear Lake volcanic field (Hammersley and DePaolo, 2006; Johnson and O'Neil, 1984; Schmitt et al., 2006).

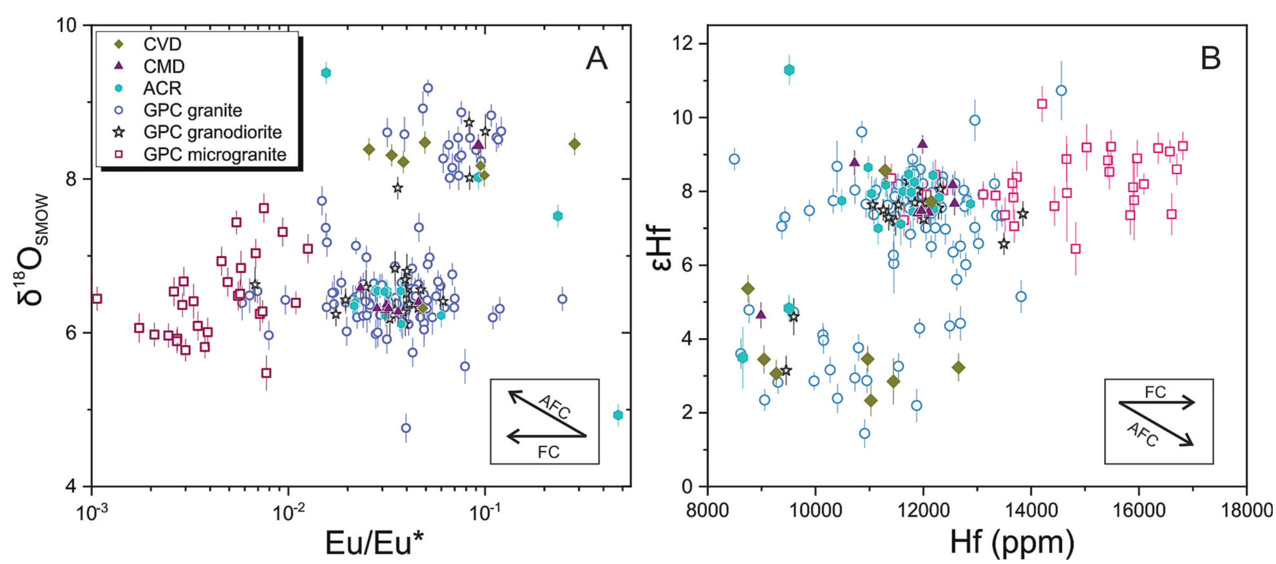

Fig. 7. Zircon O isotopes vs. Eu/Eu* (A), and zircon Hf isotopes vs. Hf (B) for GPC and CMVC units. Note that Eu/Eu* and Hf are indices of fractionation, with Eu/Eu* decreasing and Hf increasing with higher degrees of fractionation. Arrows indicate schematic trends for fractional crystallization (FC) and assimilation coupled with fractional crystallization (AFC).

3.3. Thermal models

Initial models explored a steady recharge history for a c. 900 ka interval of evolved magma presence that is constrained by average zircon ages for each well sample between c. 2.0 and 1.1 Ma (Schmitt et al., 2003b;) at uniform recharge rates of 0.1, 0.3, and 1 km^3/ka. A recharge rate < 0.1 km^3/ka will produce an intrusion with a volume smaller than the known extent of the GPC and would therefore be unrealistic. Time-invariant recharge results in steady zircon crystallization after an initial incubation period, but contrasts with the observed hiatus in the zircon ages between c. 1.5 and 1.6 Ma (Fig. S4). Moreover, the resulting Δt (which decreases with increasing recharge rate from c. 374 to 281 ka; Table 1) is less than the observed age spread. Consequently, models with a uniform recharge rate (single-stage) were abandoned in favor of two-stage models that reflect the evolution of the GPC where emplacement of the shallow microgranite predated the subsequent intrusion of the granite and granodiorite. The conspicuous absence of zircon recycling from the microgranite by the subsequently intruded granite and granodiorite (and as well in the CMVC lavas) places important constraints on two-stage models: if the volume of the initially intruded magma system up to the time of magma extraction that formed the microgranite was too high, a large amount of zircon would be produced. These zircons would inevitably become recycled during subsequent extraction of the GPC granite and granodiorite magmas because a large intrusion would remain hot, and the magma including its zircon cargo would be mobile. This recycling is, however, not observed, indicating that within the magma reservoir feeding the GPC, zircon crystallizing from a large-volume second pulse must grossly outweigh zircon generated during the first stage, when a comparatively small and cool intrusion was formed that only produced insignificant amounts of zircon compared to the later growth stage of the magma system (Fig. 8).

Trying to match separate, quasi-continuous zircon age distributions for both populations, zircon from the GPC microgranite and the granite-granodiorite, two distinct, but invariable recharge rates were explored over the 900 ka model run-time. For modelling zircon in the microgranite (Fig. S5A), recharge rates >0.1 km^3/ka result in a model intrusion that is too hot to produce zircon during the early stages, whereas recharge at the minimum rate of 0.1 km^3/ka matches the actual distribution in Δt. A good fit between model and data is obtained when the magma system initiated at 2.110 Ma. The observed Δt in zircon from the GPC granite and granodiorite (195 ka) is slightly longer than that of the microgranite (181 ka; Table 1). This, and the absence of recycled older zircon, can be modelled by a brief pulse of elevated recharge between 1.61 and 1.56 Ma, resulting in a 50 ka high-flux event that approximates the timing of the observed zircon age hiatus. Whereas a modelled intrusion formed at 2 km^3/ka would cool too rapidly (within c. 57 ka) to match Δt for zircon from the GPC granite-granodiorite, a magma body emplaced at 4 km^3/ka would crystallize zircon close to the observed Δt (Table 1; Fig. S5B). At recharge rates of 6 and 8 km^3/ka, Δt increases, but more importantly the magma system would remain too hot to crystallize significant zircon by the time zircon saturation was already recorded in the GPC granite-granodiorite (Table 1; Fig. S5B). Therefore, a peak recharge rate of 4 km^3/ka is adopted as the best-fit value. Lastly, we explored recharge temperatures at 1000 and 1200 °C (covering the range of temperatures for potential parental mafic magmas, as represented by andesite of Ford Flat or basalt of Caldwell Pines) as well as

Table 1
Compilation of observational and model parameters along with zircon age distributions quantified as the age difference between the 16% and 84% percentiles (Δt). Model solutions are also displayed in figures as referenced in the last column.

Name	Recharge temperature	Geothermal gradient	Recharge rate	Start time	End time	Δt	Final volume	Figure
	°C	°C/km	km^3/a	ka	ka	ka	km^3	
Zircon ages								
All GPC units						546		9
GPC microgranite phorphyry						181		9
GPC granite and granodiorite						153		9
Single-stage								
CA1	1100	38	0.10	2010	1110	374	95	S4
CA2	1100	38	0.30	2010	1110	314	275	S4
CA3	1100	38	1.00	2010	1110	281	905	S4
1st stage: microgranite phorphyry								
MC1	1100	38	0.10	2010	1610	168	45	S5
MC2	1100	38	0.20	2010	1610	134	85	S5
MC3	1100	38	0.10	2110	1610	195	55	S5 & S6a
MC3a	1000	38	0.10	2110	1610	177	55	S6a
MC3b	1000	30	0.10	2110	1610	111	55	S6a
MC3c	1100	30	0.10	2110	1610	158	55	S6a
MC3d	1200	38	0.10	2110	1610	215	55	S6a
MC3e	1200	30	0.10	2110	1610	192	55	S6a
2nd stage: GPC granite and granodiorite								
GGI1	1100	38	2.00	1610	1560	57	100	S5
GGI2	1100	38	4.00	1610	1560	68	200	S5 & S6b
GGI2a	1000	38	4.00	1610	1560	92	200	S6b
GGI2b	1000	30	4.00	1610	1560	40	200	S6b
GGI2c	1100	30	4.00	1610	1560	54	200	S6b
GGI2d	1200	38	4.00	1610	1560	62	200	S6b
GGI2e	1200	30	4.00	1610	1560	59	200	S6b
GGI3	1100	38	6.00	1610	1560	90	300	S5
GGI4	1100	38	8.00	1610	1560	110	400	S5
Preferred model								
1st stage			0.10	2110	1610	195		
2nd stage	1110	38	4.00	1610	1560	163	275	9
post-2nd stage			0.10	1310	1110			

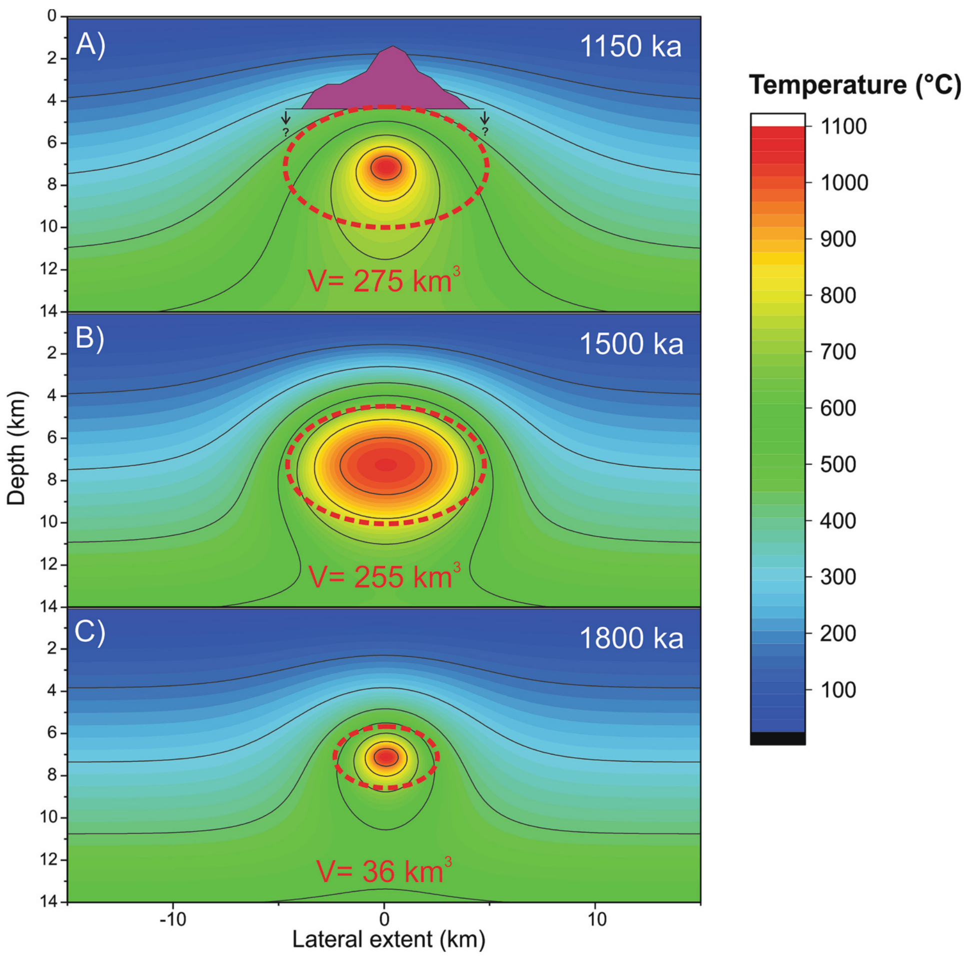

Fig. 8. Time slices for the modelled thermal evolution of the magma feeding the GPC-CMVC system at 1800, 1500 and 1150 ka (panels A to C in younging upward sequence). Panels plot central cross-sections through an ellipsoidal magma reservoir with radial symmetry where magma intrusion occurs in the center (0 km lateral extent, 7 km depth). Outlines of the total intruded volumes are indicated by dashed lines; panel A) also compares the outline of the GPC in a N-S profile with the final dimensions of the underlaying intrusion at the end of the model run. Note that the actual model dimensions (lateral extent = 60 km; depth = 20 km) are larger than the plotted range.

different initial geothermal gradients (30 and 40 °C), and only found minor effects for magma cooling during the second, high-flux, phase (Table 1; Fig. S6). For the initial phase, better fits are observed for higher magma temperatures or geothermal gradients, but given the small contribution of this phase to the overall magma volume, these parameters are of second-order importance. In the preferred model (Table 1; Fig. 9), a slightly better fit is obtained when (1) stage 1 starts at 2.11 Ma with 0.1 km^3/ka for 500 ka, and (2) stage 2 initiates with a high flux event at 1.61 Ma, followed by an intermittent shut-down at 1.56 Ma, and then resuming recharge at a low recharge rate of 0.1 km^3/Ma that is maintained between 1.31 and 1.11 Ma. This model scenario is consistent with the timing of volcanism in the CMVC, and thus geologically more reasonable than a complete shut-down of magma recharge after 1.56 Ma.

Model results can also be qualitatively compared to the thermochemical indices recorded by GPC zircon crystals. The modelled thermal evolution of the intrusive complex from which GPC and CMVC magmas were extracted shows protracted thermal stability during stage 1, followed by a thermal excursion and then a gradual temperature decline. This is consistent with the low but constant temperatures in zircon from the GPC microgranite, whereas higher and more heterogeneous temperatures are observed for GPC granite and granodiorite zircon (Fig. S7). Similarly, the more diverse and crustally influenced isotopic compositions of zircon from GPC granite and granodiorite compared to microgranite zircon agree with the expected thermal maturation of the crust following the high-flux event. With this preferred model, a total volume of the intrusive system underlying the GPC approaching ~300 km^3 is predicted (Figs. 8 and 9). Whereas magma volumes (defined by the volume of the intrusion >700 °C) are generally low (<10 km^3) during stage 1 (microgranite porphyry intrusion), a more considerable amount of magma (~50 km^3) has accumulated by the time of the youngest zircon crystallization recorded within the GPC granite-granodiorite and CMVC units (Fig. 9, S8).

4. Discussion

4.1. Revising the volcanic-plutonic links between CMVC and GPC from a zircon perspective

Previous studies have linked individual volcanic and plutonic units based on broad geochronological equivalence as well as mineralogical and whole rock geochemical similarities (Hulen et al., 1997; Rivera et al., 2013; Schmitt et al., 2003b). For ACR zircon, the presence of two populations with distinct ages and compositions has been interpreted by Rivera et al. (2013) to result from partial remelting of older, evolved intrusions (1.38–1.24 Ma) by more primitive magma recharge that produced a dominant antecrystic population; this was followed by crystallization of a less abundant zircon population between 1.23 and 1.18 Ma, immediately before eruption of ACR. Our new trace element and O-Hf-isotopic results generally agree with this model of antecrystic recycling and late-stage reheating, but we also emphasize that recycling excluded older and highly evolved zircon from the shallow microgranite porphyry: only zircon from the GPC granite and granodiorite matches the trace elemental and isotopic range of ACR zircon (Fig. 6). This also holds for zircon from CMD and CVD, for which such data were previously lacking. Isotopic data also reveal two distinct populations among GPC and CMVC zircons that have not been previously described. Both populations are present in the younger GPC granite and granodiorite, as

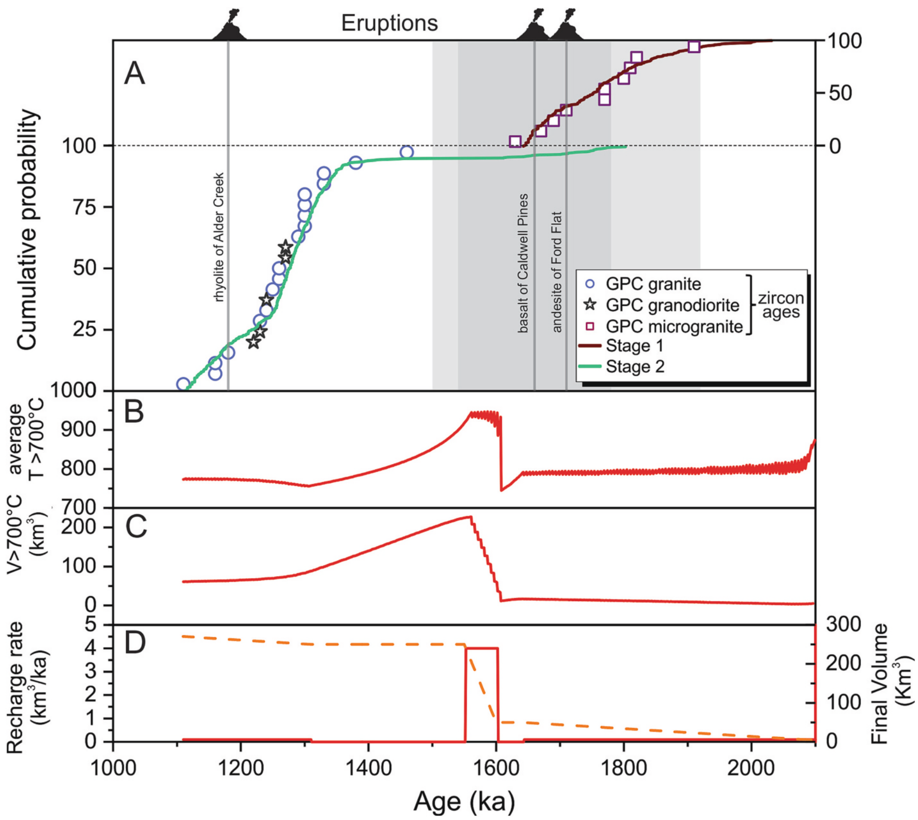

Fig. 9. Two-stage thermal model reproducing the age distribution for GPC zircon. A) cumulative probability density functions for stage 1 and 2 of the model versus the GPC zircon age averages in ranked order separated according to microgranite and granite-granodiorite units, respectively (data from Schmitt et al., 2003b). Panels below show the temporal evolution of B) average magma temperature (>700 °C), C) volume of magma above the solidus (>700 °C), and D) prescribed magma recharge rate (red solid line) with the resulting cumulative volume of the intrusion (orange dashed line). The preferred model (see text) starts with steady recharge of 0.1 km^3/ka at 2110 ka for 500 ka and is followed by higher recharge of 4 km^3/ka for 50 ka. After an episode of zero recharge dominated by magma cooling, the model returns to a steady recharge of 0.1 km^3/ka after 1310 ka. Critical eruptions within the GPC-CMVC area are indicated by vertical bars and volcano symbols on top. (For interpretation of the references to colour in this figure legend, the reader is referred to the web version of this article.)

well as in all CMVC units, whereas only one population (showing less crustal influence) was detected in the microgranite porphyry. Collectively, these observations indicate that the microgranite porphyry itself was too cold for remelting and recycling of zircon, and/or too small to have delivered any significant amount of zircon antecrysts during the main CMVC stage. The exception may be the pre-ACR explosive eruption (sample CM-04-01) preserved in limited outcrops underneath ACR lavas (unit "rap" in Hearn et al., 1995). In comparison to ACR zircon, U abundances in this sample are elevated, and U-Th-Pb ages overlap with those of microgranite porphyry (Fig. S3). Although the eruption age of this unit remains unconstrained, its zircon crystallization age would be consistent with it being a small-volume eruptive equivalent of the microgranite porphyry.

4.2. Significance of fractional crystallization vs. assimilation and implications for the GPC magma system

The increasing thermal and compositional complexity of zircon in the GPC granite-granodiorite and CMVC units compared to the microgranite porphyry implies a maturation of the magma system where fractional crystallization and assimilation progressed at different rates. In general, magmas tapped by volcanoes in the Coast Ranges of northern California evolved via coupled fractional crystallization and crustal assimilation that has been quantified in different AFC scenarios (Dickinson, 1997; Hammersley and DePaolo, 2006; Johnson and O'Neil, 1984; Schmitt et al., 2006). Multiple stages of assimilation are evident, with basaltic to basaltic andesites acquiring hybrid isotopic signatures through efficient lower-middle crustal assimilation (Hammersley and DePaolo, 2006; Schmitt et al., 2006). Xenoliths in mafic lavas support that most crustal assimilation occurred primarily at lower to mid-crustal depths (Hearn Jr et al., 1981; Stanley and Blakely, 1995; Stimac, 1993). This was typically followed by a second stage where dacitic to rhyolitic magmas evolved via upper crustal fractional crystallization where assimilation became only significant when high temperatures prevailed (Hammersley and DePaolo, 2006; Schmitt et al., 2006). Magma differentiation at shallow levels also involved remelting of previous intrusions due to renewed magma input (Rivera et al., 2013; Schmitt et al., 2006).

The thermochemical and isotopic variability of GPC-CMVC zircon indicates that magmatic heterogeneity existed in evolved melts that were zircon saturated during storage in an upper crustal magma reservoir, as suggested by the AFC model curve for Hf being compatible (Fig. 6). This heterogeneity implies thermal maturation of a long-lived magma system undergoing frequent recharge of more primitive, hot magma (basaltic to andesitic in composition) where country rocks eventually became sufficiently heated to facilitate their assimilation even at shallow crustal depths. Interestingly, the chemically least evolved CVD lava contains a comparatively large percentage of highly crustally influenced zircon, suggesting that magma recharge efficiently remobilized part of intrusive system that had previously assimilated country rock. This hints at a magma reservoir open for episodic recharge below the depth of the GPC, because the GPC itself was emplaced into cold country rock where assimilation would be negligible. Such a scenario is supported by the rapid cooling of the GPC as indicated by K-feldspar thermochronology, revealing that the GPC was magmatically short-lived, although the underlying magma system from which the GPC was fed had a more protracted lifespan (Dalrymple et al., 1999). The absence of shallow GPC rocks underneath the CMVC also favors that the source for these magmas was below the known GPC.

Microgranite porphyry zircons are isotopically uniform and equivalent to the dominant zircon population in GPC granite-granodiorite and CMVC rocks, but nonetheless they crystallized from unusually highly evolved melts as indicated by their extremely low Eu/Eu*, high incompatible trace element abundances (e.g., Y, Hf, and U), and low TiZr temperatures. Decoupling of fractional crystallization and assimilation implies magma residence at upper crustal levels where additional crustal input beyond the first stage of mid-lower crustal assimilation (sensu Hammersley and DePaolo, 2006) was largely precluded, at least during the early evolutionary stages of the system. Therefore, it is concluded that the upper crustal magma reservoir was initially small and comparatively cold during the formation of the microgranite porphyry, and only subsequently waxed into a larger system capable of producing a wider range of melt compositions along with locally elevated crustal inputs. This growth spurt of the magma system postdates the emplacement of the microgranite porphyry at c. 1.6 Ma, which is consistent with the c. 1.66 Ma age of basalt of Caldwell Pines, where mafic magma seemingly ascended to the surface without becoming trapped in the subsurface by a large, partially molten and therefore low-density magma reservoir (Fig. 9). Other regional volcanic events during the lifespan of the GPC-CMVC system comprise the early, c. 2.2 Ma and 1.7 Ma extrusions of rhyolite of Pine Mountain and andesite of Ford Flat, respectively, both to the southeast of the GPC-CMVC. Although these centers may not be directly related to the GPC, their ages agree with the inferred onset of GPC emplacement as well as a potential high-flux episode at c. 1.6 Ma as developed in the model, respectively. Dacite of Tyler Valley with an eruption age of c. 0.67 Ma, by contrast, is significantly younger than the GPC, and due to the lack of zircon of such young age in GPC-CMVC rocks, the model is unconstrained after c. 1.1 Ma. The eruption of dacite of Tyler Valley just outside the northwestern margin of the steam field, however, is consistent with higher temperatures purportedly associated with young intrusive activity in the geothermal reservoir in this direction (Peacock et al., 2020).

4.3. Geological implications from thermal models of the GPC magma system

Models seeking to explain the thermal anomaly of The Geysers invoked a long-lived magma chamber emplaced at mid crustal depths (e.g., Dalrymple et al., 1999; Isherwood, 1981). Although emplacement of a single, large plutonic body at shallow depth would generate a highly elevated geothermal gradient satisfying the conditions within the modern steam field, this thermal anomaly would be transient over timescales that are much shorter than indicated by radiometric ages for the GPC (Dalrymple et al., 1999; Norton and Hulen, 2001; Schmitt et al., 2003b). Repeated injections of magma would extend the duration of a thermal anomaly, and even though multiple phases of emplacement have been recognized based on mineralogical, geochemical, and geochronological differences within the GPC (Dalrymple et al., 1999; McLaughlin, 1981; Schmitt et al., 2003b; Stanley et al., 1998; Stimac et al., 2001), their collective ages are still too old to maintain current conditions of elevated heat flow. The notion that the GPC itself is too shallow and too small for protracted release of magmatic heat is also supported by K-feldspar thermochronometry indicating that the GPC had already cooled to <350 °C within a few 100 ka after its emplacement (Dalrymple et al., 1999). Rapid cooling of the GPC also supports that zircon with a comparatively large age span (>200 ka for the GPC granite-granodiorite and ACR volcanics as independently indicated by SIMS and TIMS data, respectively; Rivera et al., 2013; Schmitt et al., 2003b) could not have formed in-situ, but rather crystallized in a long-lived magmatic environment, where melts were sufficiently evolved to become zircon saturated and thermal conditions were conducive for the extended presence of melt.

Our model results imply that an intrusive body of nearly 300 km^3 had accumulated by 1.1 Ma, (Figs. 8 and 9), the youngest U-Th-Pb zircon age for the GPC encountered in a shallow dike (Schmitt et al., 2003b). This intrusive body represents the common magma source for the GPC and CMVC. Volume estimates for this body are conservative because of the selected model parameters where (1) new magma recharge is always emplaced in the central, and therefore hottest, part of the magma system, minimizing heat loss to the surroundings, and (2) the intrusion has an ellipsoidal shape and thus a comparatively low surface to volume ratio, (3) the model is only constrained to the youngest zircon ages in GPC-CMVC rocks of c. 1.1 Ma; subsequent intrusions such as the likely rejuvenation of the magma system that led to the eruption of the ACR, CMD, and CVD units (~5 km^3) happened at the end of the modelled interval and were thus not recorded by the accessible zircon populations. Assumptions (1) and (2) translate into slower cooling of the intrusion compared to other geometries, e.g., where a magma body is formed by stacking sills displacing country rock downward and thus always exposing the newest recharge to colder, shallower rocks (Annen et al., 2001). Thin sills also have high surface to volume ratios, so that they solidify quickly. Although our model geometry is schematic, the results broadly match geological constraints: the extent of the residual intrusive ellipsoid after extraction of ~75 km^3 of magma forming the GPC and ~ 5 km^3 of CMVC lava is ~200 km^3, broadly encompassing the area covered by the GPC and the CMVC when projected towards the surface (Fig. 2). Alternative geometries for the model intrusion are conceivable, for example by trying to match the NW-SE extension of the GPC which is likely controlled by transtension between regional faults (Stanley et al., 1998). However, in the absence of firm constraints on the geometry of the GPC beyond its drilled extent, we deem such efforts premature.

Previous estimates of GPC volumes beyond its known extent from drill well penetration were derived from extrapolating the known geometry to greater depths (e.g., 4.4 km), yielding an estimate of ~300 km^3 (Norton and Hulen, 2001), about three times the total erupted volume of the Clear Lake volcanic field (>100 km^3; Donnelly et al., 1981). Magma recharge rates for the Clear Lake area have been estimated at 2–3 km^3/ka (Hammersley and DePaolo, 2006) or 10 km^3/ka mantle input (Shaw, 1985), with a fraction of this corresponding to the production of felsic magma (~10%; Shaw, 1985). Our modelled time-integrated recharge rate of 0.1 km^3/ka is consistent with these estimates, but we emphasize that zircon age distributions and compositional diversity were only matched by varying this rate substantially with time. Our best-fit model implies a brief interval of high magma flux (4 km^3/ka for 50 ka) that was preceded and followed by intrusive accumulation at low flux (0.1 km^3/ka). Because our model is only concerned with the duration of known zircon crystallization in GPC-CMVC rocks, we cannot add any new direct insights relating to the question of the heat source for the modern geothermal system, but continuous low-flux activity over the past 1 Ma would be consistent with the notion that high heat flux was maintained or rejuvenated by multiple, smaller (possibly mafic) intrusions at depths below the GPC (e.g., Dalrymple et al., 1999).

Time-transgressive volcanism and elevated crustal heat flow following the northward migration of the Mendocino triple junction has long been recognized as a hallmark of volcanism in the California Coast Ranges (Dickinson and Snyder, 1979; Johnson and O'Neil, 1984; Lachenbruch and Sass, 1980). Oblique convergence of the Pacific-Farallon ridge-transform plate boundary system opened a slab window underneath the western margin of North America (Furlong and Schwartz, 2004) where influx of hot asthenosphere from the former mantle wedge in the wake of northward migration of the subducting Gorda slab heated the overlying continental margin and triggered volcanism (Furlong and Schwartz, 2004). Coast Range volcanism thus forms an array of progressively younger fields that track the northward migrating Mendocino triple junction (e.g., Sweetkind et al., 2011; Fig. 1). Although reconstruction of the timing of volcanic activity within individual fields is complicated by their dissection along the San Andreas fault system, the onset of volcanism appears to be delayed by approximately 3 Ma after passage of the triple junction, corresponding to a 90–110 km distance between the volcanic focus and the southern edge of the slab (Furlong and Schwartz, 2004; Sweetkind et al., 2011). During this time span, the influx of asthenosphere-derived mafic melts, characteristically with an arc signature due to prior modification of the mantle wedge, produced transcrustal magma systems, where parental magmas evolved through processes of fractional crystallization coupled with crustal assimilation as described above (Hammersley and DePaolo, 2006; Schmitt et al., 2006). Within the best preserved and least dissected volcanic outcrops of the California Coast Ranges, comprising the <12 Ma Tolay, Sonoma, and Clear Lake volcanic fields, volcanic activity lasted for c. 2–4 Ma at each location (e.g., Fox et al., 1985; Sweetkind et al., 2011; Wagner et al., 2011). The time-volume relations for individual fields, however, remain poorly constrained, but our modelling results hint at an important role of short-lived magmatic flare-ups in the evolution of these fields. In the case of the Clear Lake volcanic field, a brief high-flux event may have formed the main body of the GPC and the coeval CMVC, with most of the magmatic input retained in an intrusive complex underlying the GPC. We speculate that the older fields display a similar pattern of brief high-flux episodes within a much longer interval of volcanic background activity. Intriguingly, three widespread tephras erupted from calderas within the Eastern Sonoma volcanic field, with deposits of the voluminous Lawlor Tuff recorded in basins as far as the lower Colorado River (Harvey, 2014). These caldera-forming eruptions occurred within a comparatively brief interval (Lawlor Tuff: 4.84 Ma, Huichica tuff: 4.76 Ma, and tuff of Napa: 4.70 Ma; Sarna-Wojcicki et al., 2011) relative to the overall lifespan of the Eastern Sonoma volcanic field (c. 5.4–2.8 Ma; Sweetkind et al., 2011). This corroborates our suspicion that the crustal thermal evolution above the expanding slab window opened only a brief window of opportunity for the accumulation of voluminous (>100 km^3) silicic magma bodies that were capable of feeding sizable shallow intrusions (as for the GPC), or large-volume eruptions (as for the Eastern Sonoma calderas).

5. Conclusions

Zircon trace elements and isotopes for GPC and CMVC show considerable overlap, implying that they share a common magmatic source. This source magma system evolved by fractional crystallization independent of its degree of assimilation, which is typical for an intrusion surrounded by comparatively cold country rock. Highly negative Eu anomalies that systematically co-vary with elevated incompatible trace element (e.g., Y, Hf, and U) abundances in zircon and low TiZr temperatures indicate that the oldest unit, GPC microgranite, originated from a highly differentiated melt. Conversely, a distinct zircon population with elevated δ^{18}O and low εHf is exclusively present in the younger population of GPC and CMVC units, implying that assimilation of Franciscan Complex country rock by evolved, zircon-crystallizing magmas only became possible after the magma system achieved thermal maturity. Thermochemical modelling based on GPC zircon crystallization age distributions suggests a final volume of ~300 km^3 for the source magma system, which dominantly accumulated during a single high-flux episode at c. 1.6 Ma, when recharge rates peaked at 4 km^3/ka for 50 ka. Following this event, crustal assimilation increased in parts of the magma system where a subpopulation of younger zircon crystallized with distinctly elevated δ^{18}O and more crustally influenced εHf values. The absence of zircon carried over from the microgranite porphyry into younger GPC granite and granodiorite as well as CMVC lavas implies that the source magma system was still comparatively small during the microgranite porphyry stage. During this early stage, mafic magma recharge at 0.1 km^3/ka maintained conditions in a deeper magma reservoir suitable for low-temperature zircon crystallization in evolved melts for c. 500 ka that later would ascend to form the shallow cap of the GPC. Another upward migration of magma, this time after the reservoir increased massively in volume at c. 1.6 Ma, was then responsible for intrusion of the GPC granite and granodiorite units. Finally, the system returned to a background magma influx, where emplacement of small intrusions could be responsible for the modern geothermal anomaly (e.g., Peacock et al., 2020). Peak magma production rates in the California Coast Ranges, however, appear to be limited to a time interval much briefer than the longevity of individual volcanic fields established above a migrating slab window.

Supplementary data to this article can be found online at https://doi.org/10.1016/j.chemgeo.2023.121414.

Declaration of Competing Interest

The authors declare that they have no known competing financial interests or personal relationships that could have appeared to influence the work reported in this paper.

Data availability

Data are provided in supplement

Acknowledgments

We thank CALPINE corporation (Stephen DeOreo, Craig Hartline) for sharing data for the top of the GPC, and give credit to former CALPINE geologist Mark Walters, who passed away in July 2020, for his contributions. We also thank journal reviewers Seth Burgess and Calvin Miller for supportive comments. This is FIERCE contribution No. 123.

References

Aalto, K., 2014. Examples of Franciscan complex mélanges in the northernmost California Coast Ranges, a retrospective. Int. Geol. Rev. 56, 555–570.

Annen, C., Lénat, J.-F., Provost, A., 2001. The long-term growth of volcanic edifices: numerical modelling of the role of dyke intrusion and lava-flow emplacement. J. Volcanol. Geotherm. Res. 105, 263–289.

Barboni, M., Boehnke, P., Schmitt, A.K., Harrison, T.M., Shane, P., Bouvier, A.S., Baumgartner, L., 2016. Warm storage for arc magmas. Proc. Natl. Acad. Sci. 113 (49), 13959–13964.

Barth, A.P., Wooden, J.L., 2010. Coupled elemental and isotopic analyses of polygenetic zircons from granitic rocks by ion microprobe, with implications for melt evolution and the sources of granitic magmas. Chem. Geol. 277 (1–2), 149–159.

Beall, J., Wright, M., 2010. Southern extent of The Geysers high temperature reservoir based on seismic and geochemical evidence. Geotherm. Resourc. Council Trans. 34, 1199–1202.

Bell, E.A., Boehnke, P., Barboni, M., Harrison, T.M., 2019. Tracking chemical alteration in magmatic zircon using rare earth element abundances. Chem. Geol. 510, 56–71.

Bertani, R., 2012. Geothermal power generation in the world 2005–2010 update report. Geothermics 41, 1–29.

Caricchi, L., Simpson, G., Schaltegger, U., 2014. Zircons reveal magma fluxes in the Earth's crust. Nature 511, 457–461.

Castillo, D.A., Ellsworth, W.L., 1993. Seismotectonics of the San Andreas fault system between Point Arena and Cape Mendocino in northern California: Implications for the development and evolution of a young transform. J. Geophys. Res. Solid Earth 98, 6543–6560.

Chauvel, C., Lewin, E., Carpentier, M., Arndt, N.T., Marini, J.C., 2008. Role of recycled oceanic basalt and sediment in generating the Hf–Nd mantle array. Nat. Geosci. 1 (1), 64–67.

Chelle-Michou, C., Chiaradia, M., Ovtcharova, M., Ulianov, A., Wotzlaw, J.F., 2014. Zircon petrochronology reveals the temporal link between porphyry systems and the magmatic evolution of their hidden plutonic roots (the Eocene Coroccohuayco deposit, Peru). Lithos 198, 129–140.

Cherniak, D.J., Watson, E.B., 2003. Diffusion in zircon. Rev. Mineral. Geochem. 53, 113–143.

Claiborne, L.L., Miller, C.F., Wooden, J.L., 2010. Trace element composition of igneous zircon: a thermal and compositional record of the accumulation and evolution of a large silicic batholith, Spirit Mountain, Nevada. Contrib. Mineral. Petrol. 160, 511–531.

Dalrymple, G.B., Grove, M., Lovera, O.M., Harrison, T.M., Hulen, J.B., Lanphere, M.A., 1999. Age and thermal history of the Geysers plutonic complex (felsite unit), Geysers geothermal field, California: a ^{40}Ar/^{39}Ar and U–Pb study. Earth Planet. Sci. Lett. 173, 285–298.

Dickinson, W.R., 1997. Tectonic implications of Cenozoic volcanism in coastal California. Geol. Soc. Am. Bull. 109, 936–954.

Dickinson, W.R., Snyder, W.S., 1979. Geometry of triple junctions related to San Andreas transform. J. Geophys. Res. Solid Earth 84, 561–572.

Donnelly, J.M., Hearn Jr., B.C., Curtis, G.H., Drake, R.E., 1981. Geochronology and evolution of the Clear Lake Volcanics, California. Geol. Surv. Prof. Pap. 1141, 47–60.

Ernst, W., 2015. Franciscan geologic history constrained by tectonic/olistostromal high-grade metamafic blocks in the iconic California Mesozoic-Cenozoic accretionary complex. Am. Mineral. 100, 6–13.

Ferry, J., Watson, E., 2007. New thermodynamic models and revised calibrations for the Ti-in-zircon and Zr-in-rutile thermometers. Contrib. Mineral. Petrol. 154, 429–437.

Fox, K.F., Fleck, R.J., Curtis, G.H., Meyer, C.E., 1985. Implications of the northwestwardly younger age of the volcanic rocks of west-Central California. Geol. Soc. Am. Bull. 96, 647–654.

Friedrichs, B., Schmitt, A.K., Lovera, O.M., Atıcı, G., 2021. Zircon as a recorder of contrasting magma recharge and eruptive recurrence patterns. Earth Planet. Sci. Lett. 571, 117104.

Furlong, K.P., Schwartz, S.Y., 2004. Influence of the Mendocino triple junction on the tectonics of coastal California. Annu. Rev. Earth Planet. Sci. 32, 403–433.

Geological Survey, U.S., 2017. 1/3rd arc-second Digital Elevation Models (DEMs) - USGS National Map 3DEP Downloadable Data Collection: U.S. Geol. Surv. (Accessed 2022-11-26).

Gerdes, A., Zeh, A., 2006. Combined U–Pb and Hf isotope LA-(MC-) ICP-MS analyses of detrital zircons: comparison with SHRIMP and new constraints for the provenance and age of an Armorican metasediment in Central Germany. Earth Planet. Sci. Lett. 249, 47–61.
Gerdes, A., Zeh, A., 2009. Zircon formation versus zircon alteration—new insights from combined U–Pb and Lu–Hf in-situ LA-ICP-MS analyses, and consequences for the interpretation of Archean zircon from the Central Zone of the Limpopo Belt. Chem. Geol. 261, 230–243.
Grimes, C.B., John, B.E., Kelemen, P., Mazdab, F., Wooden, J., Cheadle, M.J., Hanghøj, K., Schwartz, J., 2007. Trace element chemistry of zircons from oceanic crust: a method for distinguishing detrital zircon provenance. Geology 35, 643–646.
Hammersley, L., DePaolo, D., 2006. Isotopic and geophysical constraints on the structure and evolution of the Clear Lake volcanic system. J. Volcanol. Geotherm. Res. 153, 331–356.
Harvey, J.C., 2014. Zircon age and oxygen isotopic correlations between Bouse Formation tephra and the Lawlor Tuff. Geosphere 10, 221–232.
Hearn Jr., B.C., Donnelly-Nolan, J., Goff, F.E., 1981. The Clear Lake volcanics: Tectonic setting and magma sources, Research in the Geysers-Clear Lake Geothermal Area, Northern California, US Government Printing Office, pp. 25–45.
Hearn, B., Donnelly-Nolan, J., Goff, F., 1995. Geologic Map and Structure Sections of the Clear Lake Volcanics, Northern California.
Hulen, J.B., Nielson, D.L., 1993. Interim report on geology of the Geysers felsite, northwestern California. In: The 1993 Annual Meeting on Utilities and Geothermal: An Emerging Partnership, Burlingame, CA, USA, pp. 249–259, 10/10-13/93.
Hulen, J.B., Nielson, D.L., 1995. Hydrothermal factors in porosity evolution and caprock formation at the Geysers steam field, California–insight from the Geysers Coring Project. Earth Sciences and Resources Institute, University of Utah, Salt Lake City, UT.
Hulen, J.B., Heizler, M.T., Stimac, J.A., Moore, J.N., Quick, J.C., 1997. New constraints on the timing of magmatism, volcanism, and the onset of vapor-dominated conditions at the Geysers steam field, California. In: Proceedings of the 22nd Workshop on Geothermal Reservoir Engineering, pp. 75–81.
Isherwood, W.F., 1981. Geophysical Overview of the Geysers, Research in the Geysers-Clear Lake Geothermal Area, Northern California, pp. 83–95.
Ito, H., Tamura, A., Morishita, T., Arai, S., Arai, F., Kato, O., 2013. Quaternary plutonic magma activities in the southern Hachimantai geothermal area (Japan) inferred from zircon LA-ICP-MS U–Th–Pb dating method. J. Volcanol. Geotherm. Res. 265, 1–8.
Jennings, C.W., Gutierrez, C., Bryant, W., Saucedo, G., Wills, C., 2010. Geologic map of California: California Geological Survey, Geologic Data Map No. 2, scale 1:750,000.
Jicha, B.R., Singer, B.S., Sobol, P., 2016. Re-evaluation of the ages of $^{40}Ar/^{39}Ar$ sanidine standards and supereruptions in the western US using a Noblesse multi-collector mass spectrometer. Chem. Geol. 431, 54–66.
Johnson, C.M., O'Neil, J.R., 1984. Triple junction magmatism: a geochemical study of Neogene volcanic rocks in western California. Earth Planet. Sci. Lett. 71, 241–262.
Kemp, A.I.S., Hawkesworth, C.J., Foster, G.L., Paterson, B.A., Woodhead, J.D., Hergt, J. M., Gray, C.M., Whitehouse, M.J., 2007. Magmatic and crustal differentiation history of granitic rocks from Hf-O isotopes in zircon. Science 315 (5814), 980–983.
Kennedy, B.M., Truesdell, A.H., 1996. The Northwest Geysers high-temperature reservoir: evidence for active magmatic degassing and implications for the origin of the Geysers geothermal field. Geothermics 25, 365–387.
Kern, J.M., de Silva, S.L., Schmitt, A.K., Kaiser, J.F., Iriarte, A.R., Economos, R., 2016. Geochronological imaging of an episodically constructed subvolcanic batholith: U-Pb in zircon chronochemistry of the Altiplano-Puna Volcanic complex of the Central Andes. Geosphere 12 (4), 1054–1077.
Lachenbruch, A.H., Sass, J., 1980. Heat flow and energetics of the San Andreas fault zone. J. Geophys. Res. Solid Earth 85, 6185–6222.
Lambert, S.J., Epstein, S., 1992. Stable-isotope studies of rocks and secondary minerals in a vapor-dominated hydrothermal system at the Geysers, Sonoma County, California. J. Volcanol. Geotherm. Res. 53 (1–4), 199–226.
Lukács, R., Caricchi, L., Schmitt, A.K., Bachmann, O., Karakas, O., Guillong, M., Molnár, K., Seghedi, I., Harangi, S., 2021. Zircon geochronology suggests a long-living and active magmatic system beneath the Ciomadul volcanic dome field (eastern-Central Europe). Earth Planet. Sci. Lett. 565, 116965.
McLaughlin, R.J., 1981. Tectonic setting of pre-Tertiary rocks and its relation to geothermal resources in the Geysers-Clear Lake area. Res. Geysers-Clear Lake Geotherm. Area North. Californ. 1141, 3–23.
Milicich, S.D., Wilson, C.J.N., Bignall, G., Pezaro, B., Charlier, B.L.A., Wooden, J.L., Ireland, T.R., 2013. U–Pb dating of zircon in hydrothermally altered rocks of the Kawerau Geothermal Field, Taupo Volcanic Zone, New Zealand. J. Volcanol. Geotherm. Res. 253, 97–113.
Mooney, W.D., Weaver, C.S., 1989. Regional crustal structure and tectonics of the Pacific coastal states; California, Oregon, and Washington. Geophys. Framework Continent. U. S. 172, 129–161.
Moore, J.N., Gunderson, R.P., 1995. Fluid inclusion and isotopic systematics of an evolving magmatic-hydrothermal system. Geochim. Cosmochim. Acta 59, 3887–3907.
Moore, J.N., Adams, M.C., Anderson, A.J., 2000. The fluid inclusion and mineralogic record of the transition from liquid-to vapor-dominated conditions in the Geysers geothermal system, California. Econ. Geol. 95, 1719–1737.
NASA JPL, 2018. NASA Shuttle Radar Topography Mission Global 3 arc second. 2018, distributed by USGS EarthExplorer. https://doi.org/10.5066/F7F76B1X.
Norton, D.L., Hulen, J.B., 2001. Preliminary numerical analysis of the magma-hydrothermal history of the Geysers geothermal system, California, USA. Geothermics 30, 211–234.
Page, F.Z., Ushikubo, T., Kita, N.T., Riciputi, L., Valley, J.W., 2007. High-precision oxygen isotope analysis of picogram samples reveals 2 μm gradients and slow diffusion in zircon. Am. Mineral. 92, 1772–1775.
Payne, J.L., McInerney, D.J., Barovich, K.M., Kirkland, C.L., Pearson, N.J., Hand, M., 2016. Strengths and limitations of zircon Lu-Hf and O isotopes in modelling crustal growth. Lithos 248, 175–192.
Peacock, J.R., Earney, T.E., Mangan, M.T., Schermerhorn, W.D., Glen, J.M., Walters, M., Hartline, C., 2020. Geophysical characterization of the Northwest Geysers geothermal field, California. J. Volcanol. Geotherm. Res. 399, 106882.
Pearce, N.J., Perkins, W.T., Westgate, J.A., Gorton, M.P., Jackson, S.E., Neal, C.R., Chenery, S.P., 1997. A compilation of new and published major and trace element data for NIST SRM 610 and NIST SRM 612 glass reference materials. Geostand. Newslett. 21, 115–144.
Peck, W.H., Valley, J.W., Graham, C.M., 2003. Slow oxygen diffusion rates in igneous zircons from metamorphic rocks. Am. Mineral. 88, 1003–1014.
Rivera, T.A., Storey, M., Schmitz, M.D., Crowley, J.L., 2013. Age intercalibration of 40Ar/39Ar sanidine and chemically distinct U/Pb zircon populations from the Alder Creek Rhyolite Quaternary geochronology standard. Chem. Geol. 345, 87–98.
Sarna-Wojcicki, A.M., Deino, A.L., Fleck, R.J., McLaughlin, R.J., Wagner, D., Wan, E., Wahl, D., Hillhouse, J.W., Perkins, M., 2011. Age, composition, and areal distribution of the Pliocene Lawlor Tuff, and three younger Pliocene tuffs, California and Nevada. Geosphere 7, 599–628.
Scherer, E.E., Whitehouse, M.J., Munker, C., 2007. Zircon as a monitor of crustal growth. Elements 3, 19–24.
Schmitt, A.K., Grove, M., Harrison, T.M., Lovera, O., Hulen, J., Walters, M., 2003a. The Geysers-Cobb Mountain Magma System, California (Part 1): U-Pb zircon ages of volcanic rocks, conditions of zircon crystallization and magma residence times. Geochim. Cosmochim. Acta 67, 3423–3442.
Schmitt, A.K., Grove, M., Harrison, T.M., Lovera, O., Hulen, J., Walters, M., 2003b. The Geysers-Cobb Mountain Magma System, California (Part 2): Timescales of pluton emplacement and implications for its thermal history. Geochim. Cosmochim. Acta 67, 3443–3458.
Schmitt, A.K., Romer, R.L., Stimac, J.A., 2006. Geochemistry of volcanic rocks from the Geysers geothermal area, California Coast Ranges. Lithos 87, 80–103.
Schmitt, A.K., Stockli, D.F., Lindsay, J.M., Robertson, R., Lovera, O.M., Kislitsyn, R., 2010. Episodic growth and homogenization of plutonic roots in arc volcanoes from combined U–Th and (U–Th)/He zircon dating. Earth Planet. Sci. Lett. 295 (1–2), 91–103.
Schmitt, A.K., Klitzke, M., Gerdes, A., Schäfer, C., 2017. Zircon Hafnium–Oxygen isotope and trace element petrochronology of intraplate volcanic rocks from the Eifel (Germany) and implications for mantle versus crustal origins of zircon megacrysts. J. Petrol. 58, 1841–1870.
Schriener Jr., A., Suemnicht, G., 1980. Subsurface intrusive rocks at the Geysers geothermal area, California. Geol. Soc. Am., Abstr. Programs (United States) 12.
Shaw, H.R., 1985. Links between magma-tectonic rate balances, plutonism, and volcanism. J. Geophys. Res. Solid Earth 90, 11275–11288.
Simon, J., Reid, M., Young, E., 2005. New isotopic measurements of zircon and feldspar constrain the magmatic evolution at Long Valley Caldera. Geochim. Cosmochimica Acta Supplem. 69, A234.
Spera, F.J., Bohrson, W.A., 2001. Energy-constrained open-system magmatic processes I: General model and energy-constrained assimilation and fractional crystallization (EC-AFC) formulation. J. Petrol. 42, 999–1018.
Stanley, W.D., Blakely, R.J., 1995. The Geysers-Clear Lake geothermal area, California—an updated geophysical perspective of heat sources. Geothermics 24, 187–221.
Stanley, W.D., Benz, H.M., Walters, M.A., Villaseñor, A., Rodriguez, B.D., 1998. Tectonic controls on magmatism in The Geysers–Clear Lake region: Evidence from new geophysical models. Geol. Soc. Am. Bull. 110, 1193–1207.
Stimac, J., 1993. The Origin and Significance of High-Grade Metamorphic Xenoliths. Clear Lake Volcanics, California. In: Rytuba, J.J. (Ed.), Active Geothermal Systems and Gold-mercury Deposits in the Sonoma-Clear Lake Volcanic. Fields, California.
Stimac, J.A., Pearce, T.H., 1992. Textural evidence of mafic-felsic magma interaction in dacite lavas, Clear Lake, California. Am. Mineral. 77, 795–809.
Stimac, J.A., Goff, F., Wohletz, K., 2001. Thermal modeling of the Clear Lake magmatic-hydrothermal system, California, USA. Geothermics 30, 349–390.
Sweetkind, D.S., Rytuba, J.J., Langenheim, V.E., Fleck, R.J., 2011. Geology and geochemistry of volcanic centers within the eastern half of the Sonoma volcanic field, northern San Francisco Bay region, California. Geosphere 7, 629–657.
Tierney, C.R., Schmitt, A.K., Lovera, O.M., de Silva, S.L., 2016. Voluminous plutonism during volcanic quiescence revealed by thermochemical modeling of zircon. Geology 44, 683–686.
Trail, D., Mojzsis, S.J., Harrison, T.M., Schmitt, A.K., Watson, E.B., Young, E.D., 2007. Constraints on Hadean zircon protoliths from oxygen isotopes, Ti-thermometry, and rare earth elements. Geochem. Geophys. Geosyst. 8 (6) https://doi.org/10.1029/2006GC001449.
Trail, D., Bindeman, I.N., Watson, E.B., Schmitt, A.K., 2009. Experimental calibration of oxygen isotope fractionation between quartz and zircon. Geochim. Cosmochim. Acta 73, 7110–7126.
Valley, J.W., Kinny, P.D., Schulze, D.J., Spicuzza, M.J., 1998. Zircon megacrysts from kimberlite: oxygen isotope variability among mantle melts. Contrib. Mineral. Petrol. 133, 1–11.
Vervoort, J.D., Plank, T., Prytulak, J., 2011. The Hf–Nd isotopic composition of marine sediments. Geochim. Cosmochim. Acta 75 (20), 5903–5926.
Wagner, D.L., Saucedo, G.J., Clahan, K.B., Fleck, R.J., Langenheim, V.E., McLaughlin, R. J., Sarna-Wojcicki, A.M., Allen, J.R., Deino, A.L., 2011. Geology, geochronology, and

paleogeography of the southern Sonoma volcanic field and adjacent areas, northern San Francisco Bay region, California. Geosphere 7 (3), 658–683.
Wakabayashi, J., 2015. Anatomy of a subduction complex: Architecture of the Franciscan complex, California, at multiple length and time scales. Int. Geol. Rev. 57, 669–746.
Walters, M.A., Combs, J., 1992. Heat flow in the Geysers-Clear Lake geothermal area of northern California, USA, Monograph on the Geysers Geothermal Field. Geotherm. Resourc. Council 43–53.
Weber, G., Caricchi, L., Arce, J.L., Schmitt, A.K., 2020. Determining the current size and state of subvolcanic magma reservoirs. Nat. Commun. 11, 1–14.
Wiedenbeck, M., Hanchar, J.M., Peck, W.H., Sylvester, P., Valley, J., Whitehouse, M., Kronz, A., Morishita, Y., Nasdala, L., Fiebig, J., 2004. Further characterisation of the 91500 zircon crystal. Geostand. Geoanal. Res. 28, 9–39.
Wilson, C.J.N., Charlier, B.L.A., Fagan, C.J., Spinks, K.D., Gravley, D.M., Simmons, S.F., Browne, P.R.L., 2008. U–Pb dating of zircon in hydrothermally altered rocks as a correlation tool: application to the Mangakino geothermal field, New Zealand. J. Volcanol. Geotherm. Res. 176 (2), 191–198.